Research Article Vol. 8, No. 1 / January 2021 / Optica 15

3D diffractive imaging of nanoparticle ensembles using an x-ray laser

Kartik Ayyer,[1,2,3,*,†] P. Lourdu Xavier,[1,3,4,†] Johan Bielecki,[5] Zhou Shen,[6] Benedikt J. Daurer,[6] Amit K. Samanta,[4] Salah Awel,[4] Richard Bean,[5] Anton Barty,[4] Martin Bergemann,[5] Tomas Ekeberg,[7] Armando D. Estillore,[4] Hans Fangohr,[5] Klaus Giewekemeyer,[5] Mark S. Hunter,[8] Mikhail Karnevskiy,[5] Richard A. Kirian,[9] Henry Kirkwood,[5] Yoonhee Kim,[5] Jayanath Koliyadu,[5] Holger Lange,[3,10] Romain Letrun,[5] Jannik Lübke,[3,4,11] Thomas Michelat,[5] Andrew J. Morgan,[12] Nils Roth,[4,11] Tokushi Sato,[5] Marcin Sikorski,[5] Florian Schulz,[10] John C. H. Spence,[9] Patrik Vagovic,[4,5] Tamme Wollweber,[1,2,3] Lena Worbs,[4,11] Oleksandr Yefanov,[4] Yulong Zhuang,[1,2] Filipe R. N. C. Maia,[7,13] Daniel A. Horke,[3,4,14] Jochen Küpper,[3,4,11,15] N. Duane Loh,[6,16] Adrian P. Mancuso,[5,17] and Henry N. Chapman[3,4,11]

[1]Max Planck Institute for the Structure and Dynamics of Matter, 22761 Hamburg, Germany
[2]Center for Free-Electron Laser Science, 22761 Hamburg, Germany
[3]The Hamburg Center for Ultrafast Imaging, Universität Hamburg, 22761 Hamburg, Germany
[4]Center for Free-Electron Laser Science, DESY, 22607 Hamburg, Germany
[5]European XFEL, 22869 Schenefeld, Germany
[6]Center for BioImaging Sciences, National University of Singapore, Singapore 117557, Singapore
[7]Department of Cell and Molecular Biology, Uppsala University, 75124 Uppsala, Sweden
[8]Linac Coherent Light Source, SLAC National Accelerator Laboratory, Menlo Park, California 94025, USA
[9]Department of Physics, Arizona State University, Tempe, Arizona 85287, USA
[10]Institute of Physical Chemistry, Universität Hamburg, 20146 Hamburg, Germany
[11]Department of Physics, Universität Hamburg, 22761 Hamburg, Germany
[12]University of Melbourne, Physics, Melbourne, VIC 3010, Australia
[13]NERSC, Lawrence Berkeley National Laboratory, Berkeley, California 94720, USA
[14]Institute for Molecules and Materials, Radboud University, 6525 AJ Nijmegen, The Netherlands
[15]Department of Chemistry, Universität Hamburg, 20146 Hamburg, Germany
[16]Department of Physics, National University of Singapore, Singapore 117551, Singapore
[17]Department of Chemistry and Physics, La Trobe Institute for Molecular Science, La Trobe University, Melbourne, VIC 3086, Australia
*Corresponding author: kartik.ayyer@mpsd.mpg.de

Received 7 October 2020; revised 3 November 2020; accepted 20 November 2020 (Doc. ID 410851); published 24 December 2020

Single particle imaging at x-ray free electron lasers (XFELs) has the potential to determine the structure and dynamics of single biomolecules at room temperature. Two major hurdles have prevented this potential from being reached, namely, the collection of sufficient high-quality diffraction patterns and robust computational purification to overcome structural heterogeneity. We report the breaking of both of these barriers using gold nanoparticle test samples, recording around 10 million diffraction patterns at the European XFEL and structurally and orientationally sorting the patterns to obtain better than 3-nm-resolution 3D reconstructions for each of four samples. With these new developments, integrating advancements in x-ray sources, fast-framing detectors, efficient sample delivery, and data analysis algorithms, we illuminate the path towards sub-nanometer biomolecular imaging. The methods developed here can also be extended to characterize ensembles that are inherently diverse to obtain their full structural landscape.

https://doi.org/10.1364/OPTICA.410851

1. INTRODUCTION

The determination of the structures of biomolecules at atomic resolution requires bright sources of radiation, which are unfortunately also energetic enough to degrade the object under observation [1]. All approaches to structure determination are dedicated primarily to overcoming, or working around, the effects of this radiation damage. In x-ray crystallography, large numbers of aligned molecules amplify the diffraction signal that can be

obtained within the exposure that the sample can tolerate. The tolerable dose can be increased somewhat by cooling the crystals to cryogenic temperatures. Such cooling also allows electron microscopy—where the ratio of the image-forming to damage-causing radiation is more favorable—to record faint and noisy images of many uncrystallized molecules, which can then be used to build up a three-dimensional image. The extreme intensity and ultrashort pulses of x-ray free electron lasers (XFELs) potentially offer another way to obtain structural information from single macromolecules, but without the need for cooling [2]. Pulses of femtosecond duration can outrun radiation damage and essentially freeze the molecule in time [3,4].

Single particle imaging (SPI) at XFELs consists of collecting coherent diffraction patterns from individual particles intersecting bright XFEL pulses. Theoretical work predicts that currently available XFEL sources generate enough scattered photons from single macromolecules to solve for their unknown orientations and reconstruct 3D structures of large reproducible biomolecules [5–7]. Proof-of-principle SPI experiments on biological particles [8–14] have highlighted the challenges of the approach, i.e., the recording of a large number of patterns, all with sufficiently low background, and from structurally homogeneous samples.

Here, we present experimental results that address these challenges and show the path towards single-particle imaging of macromolecules. We overcame the first challenge by aerosol injection of gold nanoparticles (AuNPs) and collected millions of patterns by using the megahertz-rate European XFEL [15] and a relatively large illumination area of the XFEL beam. The particles were chosen for two reasons, the first being the high scattering power of gold, which balances the reduced intensity from the large beam size to provide scattering signals at the levels expected from biological materials once tight focusing is achieved. The other reason is that their inherent heterogeneity from the synthesis reflects what is expected with biomolecules, especially at higher resolutions.

To recover a high-resolution 3D structure, a structurally homogeneous dataset must be generated. This challenge was performed computationally using an extension of the well-known Expand-Maximize-Compress (EMC) algorithm [16]. Even though individual diffraction patterns contained as few as 0.0012 photons per pixel on average, we show that this is sufficient not only to extract the orientations of particles, but also to disentangle structural variations. We obtain a 3D structure approaching 2 nm resolution, which is significantly improved compared to what could be achieved without structural sorting.

With further improvements in aerosol sample delivery to increase the particle density in the x-ray focus [17–19], more highly focused x-ray beams can be used to obtain similar data from biomolecules. The computational techniques developed here also open the way to experiments that can reveal thermodynamically rare states in an ensemble and characterize heterogeneous ensembles with statistical rigor. The short exposure times set by the femtosecond pulse duration will also offer unprecedented opportunities for capturing the dynamics of macromolecules in real time.

In Section 2, we describe the experimental setup and data collection process, including observation of beam-induced melting of some samples for 1 MHz repetition rate. This is followed in Section 3 by the classification of diffraction patterns using 2D averaging and per-pattern size and incident fluence determination. Finally, 3D reconstructions are performed on subsets of the data in Section 4, showing an improvement in structure quality when the appropriate selection is performed and demonstrating the power of the serial data collection method.

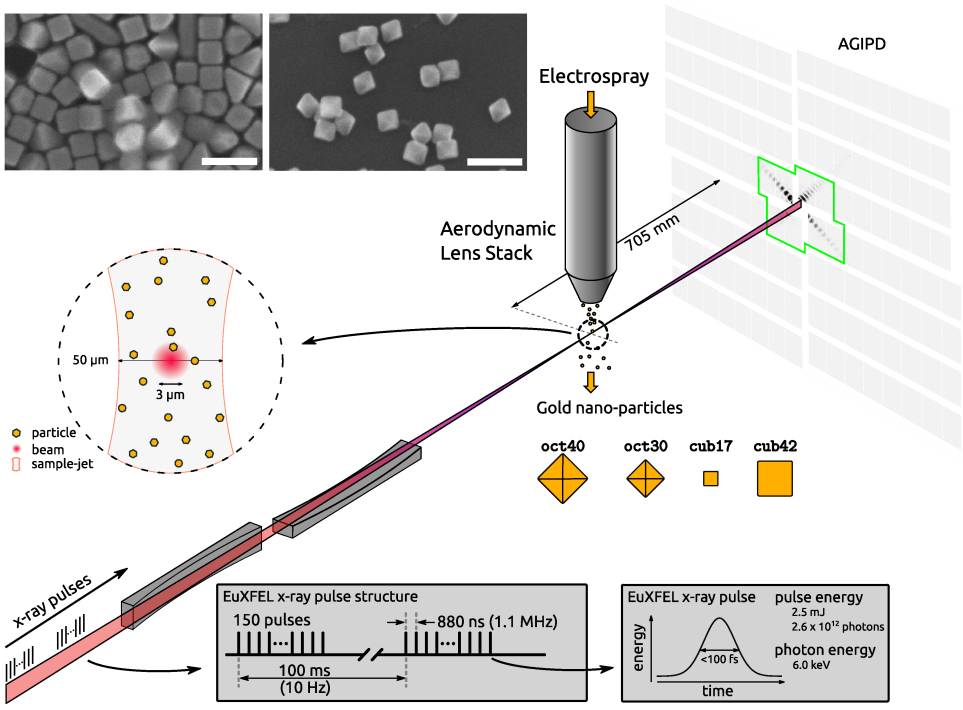

Fig. 1. Experimental setup. XFEL pulses were focused by a series of Kirkpatrick–Baez mirrors into a $3 \times 3\ \mu m^2$ spot and scattered off particles in the aerosol stream to produce diffraction patterns on the AGIPD. The lower inset shows the timing structure of the XFEL pulses at the instrument, while the top inset shows representative SEM images of the cub42 and oct30 samples; scale bars are 100 nm. The low-resolution part of the detector used for the structural sorting is highlighted in green.

Table 1. Data Collection Statistics for the Four Nanocrystal Samples[a]

Parameter	oct30	oct40	cub42	cub17
No. frames	15,805,472	29,309,832	34,197,950	36,966,286
No. hits	2,117,732	2,133,041	2,451,068	3,307,723
Hit ratio	13.40%	7.28%	7.17%	8.95%
Hits/hour	376,947	233,553	228,633	402,954
Hits/train[b]	5.2/10.4/15.6	2.8/6.4/8.4	2.4/5.6/9.1	NA/7.2/12.1
No. "good" hits	1,430,086	1,249,328	433,259	564121
Sphere fraction (%)[b]	3.4/4.0/19.2	2.7/7.2/33.5	2.4/10.4/29.1	NA[c]
Resolution (nm)[d]	3.50 (2.10-4.54)	5.32 (1.89-7.17)	4.89 (1.98-6.56)	2.11 (1.81-3.31)

[a]Sample names refer to their nominal shape (octahedron or cube) and edge length in nanometers.
[b]The three numbers correspond to values for 0.28 MHz, 0.55 MHz, and 1.1 MHz intra-train repetition rates, respectively.
[c]There was no clear sign of spherical particles for the cub17 sample.
[d]The first number is the azimuthal average resolution, while numbers in parentheses show minimum and maximum values, respectively.

2. MILLION-PATTERN DATA COLLECTION

Data was collected at the SPB/SFX (single particles, biomolecules, and clusters/serial femtosecond crystallography) instrument [20] of the European XFEL using 6 keV photons focused into a $3 \times 3\ \mu m^2$ spot, as measured by a 20 μm thick YAG screen in the focal plane. Individual x-ray pulses were generated with 2.5 mJ of energy on average (2.6×10^{12} photons). The pulses were delivered in 150-pulse trains with an intra-train repetition rate of 1.1 MHz and trains arriving every 0.1 s, leading to a maximum data collection rate of 1500 frames/second. A detector built specifically for this burst mode operation, the Adaptive Gain Integrating Pixel Detector (AGIPD) [21], was placed 705 mm downstream of the interaction region to collect the diffraction patterns for each pulse individually up to a scattering angle of 8.3° at the center-edge of the detector (Fig. 1).

Gold octahedra and cubes, each of two different sizes, were sequentially injected into the x-ray beam using an electrospray-ionization aerodynamic-lens-stack sample delivery system. The nominal sizes of the particles measured using scanning electron microscopy were 30 and 40 nm for the octahedra and 42 and 17 nm for the cubes. In the rest of the paper, these samples are described using the codes oct30, oct40, cub42, and cub17, respectively. The octahedra and cubes were prepared using different protocols, generating different heterogeneity profiles, as will be seen later.

Diffraction patterns were observed in around 10% of the collected frames. This relatively high hit ratio compared to those achieved with biological particles in similar conditions was due to a combination of the relatively large x-ray focal spot size, high particle concentration and high mass and density of the larger AuNPs, leading to lower speeds after acceleration by the gas flow in the aerodynamic lens stack [17,22,23]. Lower speeds lead to higher spatial densities, and thus higher hit ratios for the same particle beam size. Table 1 shows the statistics of the number of frames collected for each sample as well as the various filtration steps after the analyses described below.

When using the peak repetition rate of 1.1 MHz and 150 pulses per train, diffraction patterns corresponding to the shapes of cubes and octahedra could be observed, but a high fraction of the diffraction patterns appeared to originate from spherical particles (see Table 1 and third column of Fig. 2). This was found to be caused by the melting of particles in the wings of the previous XFEL pulse in the train, as the particles approached the focus. To reduce this occurrence, we therefore reduced the intra-train repetition rate from 1.1 MHz to 550 kHz, providing only half the available pulses; further reduction of the repetition rate was tested but not found to be necessary. This reduced-rate mode was used to collect most of the data for the three larger samples (but not the cub17 sample).

3. SINGLE-HIT SELECTION BY 2D CLASSIFICATION

Frames with diffraction from particles were detected by setting a threshold on the number of pixels in the AGIPD detector that recorded at least one photon. Unfortunately, not all the particles are of interest, even accounting for the heterogeneity. The extraneous patterns include those from spheres formed after melting, multi-particle aggregates, and other possible contaminants. In previous work, either manual selection [10,13] or manifold learning methods [12,24] have been used to classify patterns and reject outliers. We adopt an alternative approach, similar to one commonly used in cryo-EM [25], but implemented in diffraction space. Two-dimensional orientation determination into multiple models was performed in the detector plane using the EMC algorithm [16,26] implemented in *Dragonfly* [27]. The in-plane rotation angle (θ) and relative incident fluence (ϕ) of each diffraction pattern were determined collectively, and multiple independent 2D intensity models were reconstructed. Each of these intensities represents an average of aligned copies of a subset of the patterns from the whole set. In addition to the EMC algorithm being highly noise tolerant [7,28,29], one can also use it to examine the average models to understand what type of particles are in the dataset.

In this experiment, 50 random white noise 2D intensity models were used as initial guesses to perform the classification for each sample, using only the low resolution part of the detector highlighted at this stage (Fig. 1). Some of the reconstructed intensities are shown in Fig. 2. The first two columns of the figure show representative examples of "good" models of each sample, chosen manually to be those with high contrast and strong streaks for further processing. The third column shows an average of diffraction from rounded particles (except in the cub17 case where a dimer average is highlighted). These models were used to determine the sphere fraction shown in Table 1. Finally, the last column shows low-contrast models where a diverse set of particles was averaged.

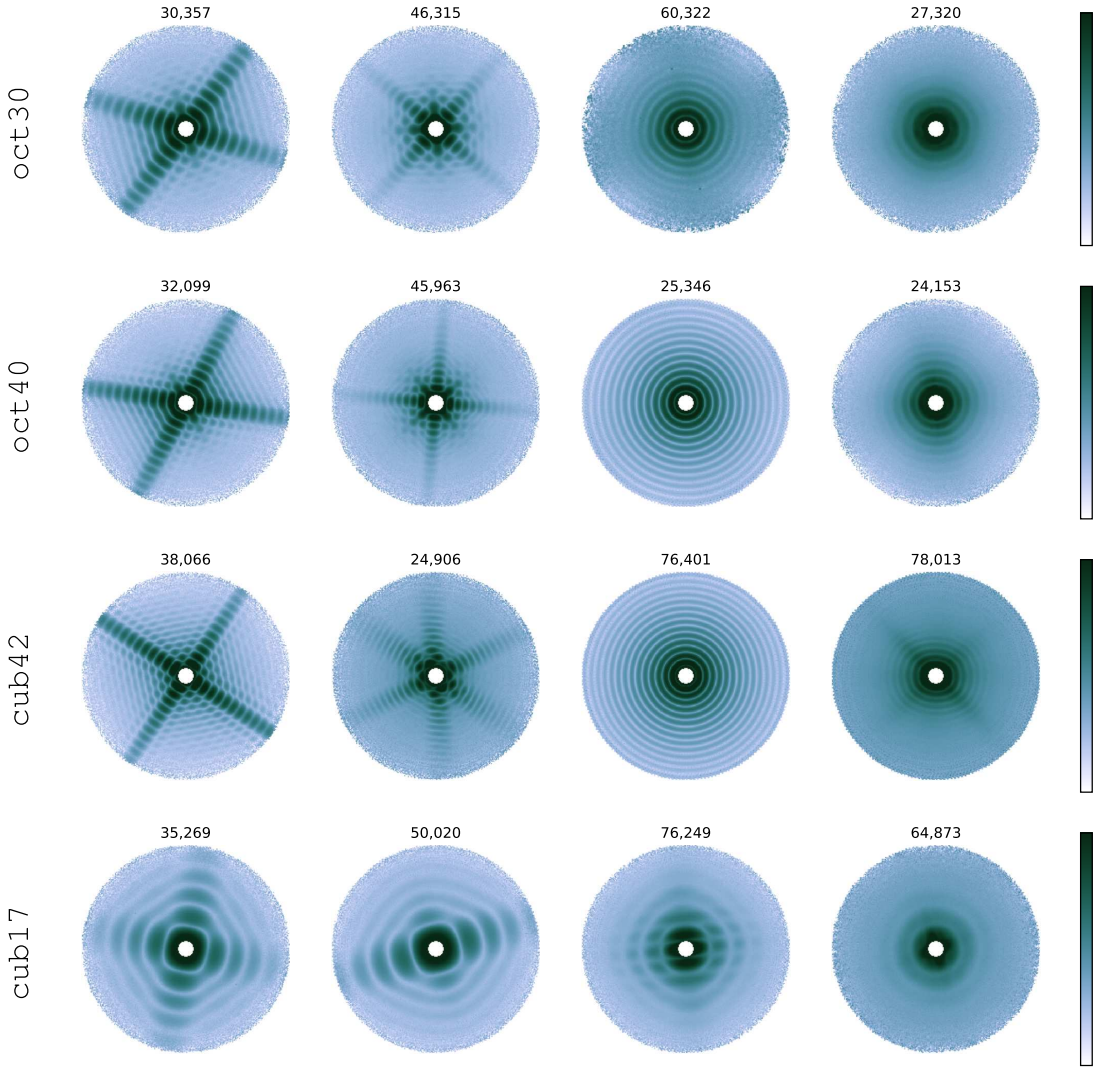

Fig. 2. 2D classification. Representative examples of reconstructed 2D models shown on a logarithmic scale, with each row representing a different sample. The numbers indicate how many patterns had that model as the most likely one. The first two columns show models selected for further processing. The third column shows diffraction from rounded/spherical particles, except in the cub17 case where there were no spherical particles and the model shows diffraction from a dimer instead. The fourth column shows some of the low-contrast models generated by averaging patterns from a diverse set of particles. The resolution at the edge of the circle is 3.3 nm.

A. Single-Shot Characterization

The 2D classification also enabled the analysis of size heterogeneity from those models where the faces of the nanoparticles were parallel to the x-ray beam. In these cases, one observes strong streaks on the detector, and the fringe spacing indicates the distance between these parallel faces. The size distributions of the samples inferred this way are shown in Fig. 3(a). The octahedral samples had a much broader size distribution than the cubic ones. While some of the breadth of the peaks is due to apparent size variations when the faces are not perfectly parallel to the beam, the much broader size distributions of the octahedra suggest that they had more heterogeneity.

In addition, the octahedra were also noticeably asymmetric, as seen in Figs. 3(c) and 3(d). These histograms were made by identifying patterns that belonged to models with two strong streaks (e.g., top left model in Fig. 2). Another run of 2D classification with just these two-streak patterns showed no variation in the angle between the streaks, but only in the fringe spacing. This is to be expected since the angle is fixed by the ⟨111⟩ growth direction, while the size is not restricted by symmetry. The equivalent figures for the cubic samples showed no asymmetry.

Due to the low polydispersity of the cubes, they were used to determine the incident fluence distribution of the x-ray beam. Since the Fourier transform of a cube is the product of three orthogonal sinc functions, the size fitting procedure also generated a predicted incident fluence. The distribution from 102,480 patterns is shown in Fig. 3(b), yielding a maximum fluence of around 60 $\mu J/\mu m^2$, which leads to a lower bound estimate of around 540 μJ in the focal spot from the measured spot size. The actual fluence was likely higher, as the particles were not ideal cubes and the scattering efficiency is reduced at high fluences [30]. One can also see that most diffraction patterns were obtained with lower incident fluences, because the particles interacted with the outer regions of the x-ray focus. The expected behavior of a Gaussian focal spot is shown as a red dashed line and shows a much

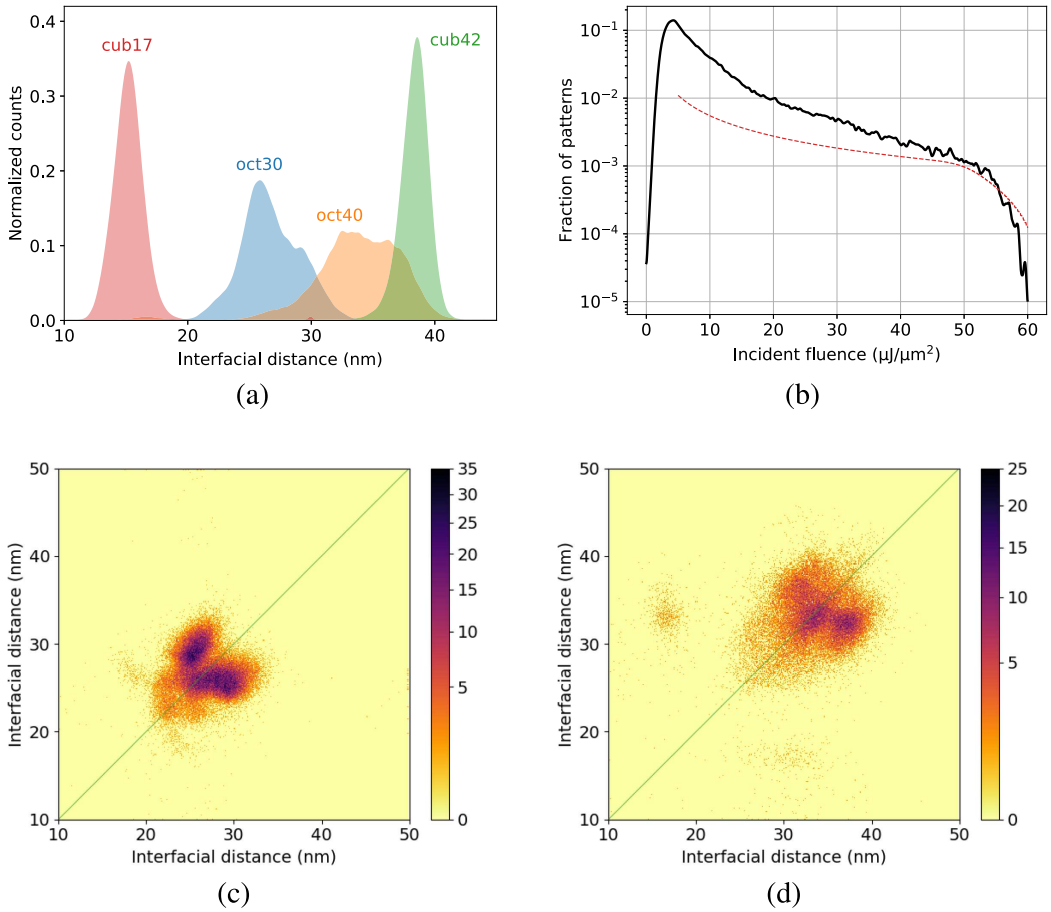

Fig. 3. Size and incident fluence distributions from 2D classification. (a) Size distribution for the four samples. The sizes are represented by the distance between opposing parallel faces. The cubes have narrow distributions, while the octahedral distributions are broader. (b) Distribution of incident fluence on the particle calculated from the cub42 sample assuming they are ideal cubes. The red dashed line represents the expected behavior from an ideal Gaussian focus weighted by the measured pulse energy distribution. (c), (d) 2D histogram of size distributions from two-streak patterns for the oct 30 and oct 40 samples, respectively. High density in the off-diagonal regions suggests the particles are asymmetric. The horizontal axis represents the brighter of the two streaks.

lower fraction of weak hits [31]. This difference can be accounted for by the stronger wings of the x-ray focus than for a Gaussian spot, which are also responsible for the melting observed at high repetition rates.

4. 3D RECONSTRUCTION WITH STRUCTURAL SORTING

The fraction of good hits used for 3D structure reconstruction varied from 17% for the cube samples to around 60% for the octahedra (Table 1). The 3D intensity distribution was obtained using these patterns before recovering the structures by performing phase retrieval using a combination of the difference map and error reduction algorithms [7]. For computational efficiency, the 3D orientations were first determined using the low-resolution part of the detector where the corner resolution was 3.3 nm. A refinement procedure similar to that developed for serial crystallography with the EMC algorithm [32] was used with the whole detector to get the full-resolution 3D intensities. In this procedure, only orientations in the neighborhood of the most likely orientation of a given pattern from the low-resolution run were searched.

A. Octahedral Samples oct30 and oct40

For the octahedra, the results from this conventional single-model approach are shown in Fig. 4(a). The intensities have noticeably lower contrast than the equivalent slices in the 2D models. From the size distributions seen in Fig. 3, this could be attributed to structural heterogeneity. To counter this, the patterns were probabilistically partitioned into five intensity volumes in a manner equivalent to the 2D classification procedure. However, the initial guesses were not random white noise, but rather isotropically stretched/scaled versions of the single model reconstructed above. Five models, with stretch factors ranging from 0.9 to 1.1 were used as these initial seeds. The rest of the reconstruction proceeded without any restraints between these models or any symmetry constraints.

Once again, this structural sorting was performed at low resolution before refining the orientations of a subset of patterns from a single model to get full-resolution intensities. Slices through the 3D intensity for the oct30 sample are shown in Fig. 4(a). The left column, showing the single-model reconstruction with 1.4 million patterns has noticeably worse fringe contrast and background than the equivalent slices in the right column or in the first two columns of the 2D classification output shown in Fig. 2. The homogeneous

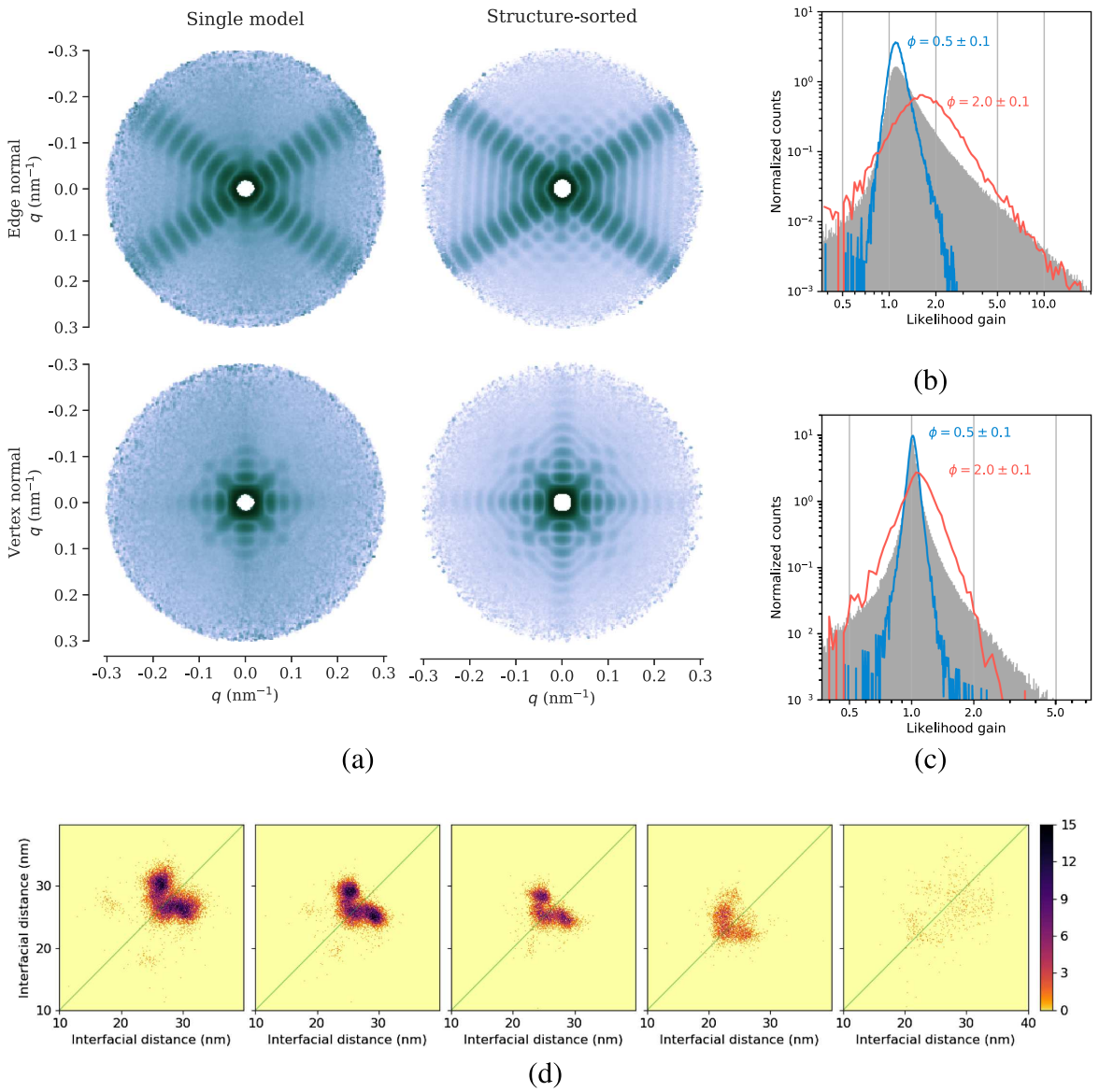

Fig. 4. Effect of structural sorting. Comparison of 3D intensity reconstructions for the octahedra before and after structural sorting. (a) Low-resolution logarithmic intensities of the oct30 sample comparing the standard single-model reconstruction with one of the sorted models. The two rows represent slices normal to an edge and vertex of the octahedron. (b) Likelihood gain distribution for the patterns shared with the sorted model shown in (a). The blue and red curves show distributions for weak and strong patterns, as identified by the relative fluence factor ϕ, respectively. (c) Same gain plot for the oct40 sample. (d) Two-streak size histograms [Fig. 3(c)] for the oct30 sample separated into the five reconstructed models.

set had 0.53 million patterns selected using the multi-model EMC reconstruction. The visual improvement is accompanied by an increase in likelihood of the model intensities outside the central speckle for the common patterns in both sets, as shown in Fig. 4(b). The filled histogram shows the distribution of the per-pattern increase in likelihood, which we refer to as likelihood gain (see Supplement 1, Section 6), while the two traces show the distributions for weak (relative scale 0.5 ± 0.1) and strong (relative scale 2.0 ± 0.1) patterns. The latter shows how brighter patterns are more selective towards an improved model. Figure 4(c) shows the same information for the oct40 sample, where the gain ratio is smaller, but still greater than one. The 2D size distributions shown in Fig. 3(c) were re-calculated for each subset of patterns belonging to the five models and plotted in Fig. 4(d), confirming the different sizes for each model, but also exhibiting a simpler structure than that of the full dataset.

B. Cubic Samples cub42 and cub17

For the cubic particles, a single-model 3D reconstruction was deemed sufficient, due to the relative monodispersity of the sample. The selection of good hits from the 2D classification was more stringent, including only high-contrast cube-like patterns. The incident fluence factors were estimated in the first few iterations where the calculated probability distributions were broad and then later kept fixed (see Supplement 1).

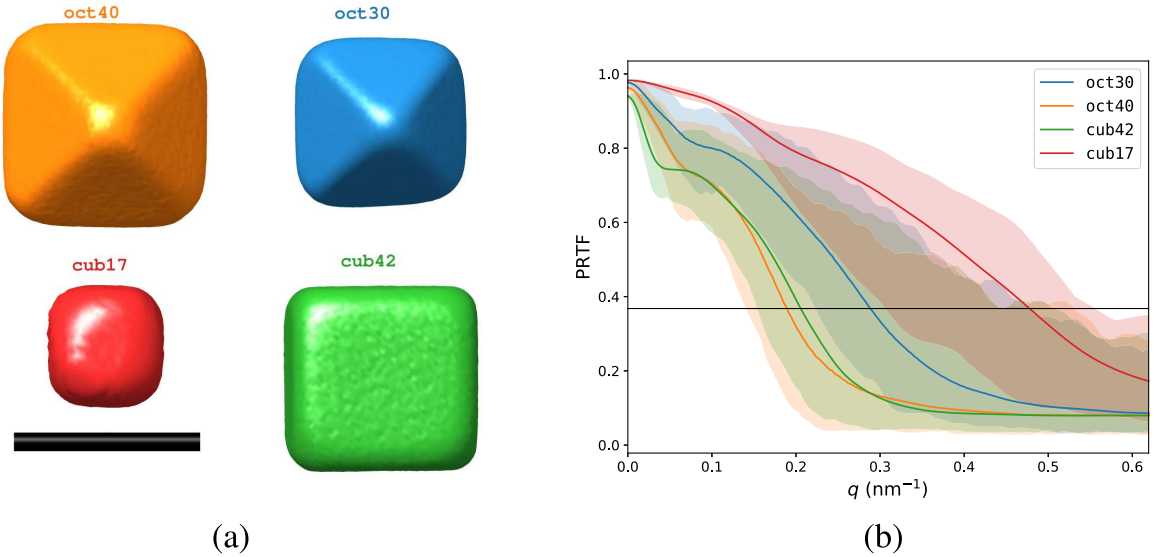

Fig. 5. Phase retrieval. (a) Isosurface plots of electron densities recovered after phase retrieval (scale bar is 40 nm). The asymmetric structures of the octahedra are clearly evident (see Visualization 2 and Fig. S7). (b) Smoothed phase retrieval transfer function (PRTF) measuring reproducibility of phases as a function of q. The solid lines represent the azimuthal average PRTF conventionally used to determine the resolution of the structure. The shaded region around each line indicates the range of values at each q. The typical $1/e$ cutoff is shown in black.

C. Phase Retrieval

The electron densities were reconstructed by performing 3D iterative phase retrieval on the full-resolution intensity volumes (see Visualization 1 for details and Fig. S6 for intensity slices). Figure 5(a) shows the reconstructed electron densities as isosurface plots. The contour levels were chosen where the gradient of the density was highest. Other views of the particles are shown in Fig. S7. The phase retrieval transfer function (PRTF) metric as a function of wave-vector q is shown in Fig. 5(b). This metric is a measure of the reproducibility of recovered phases when starting from 128 random models. The 3D PRTF distribution was smoothed using a Gaussian kernel with a width equal to one-third of the fringe width. The shaded region around each line shows the range of values in each q shell, highlighting the strong anisotropy of the metric due to the faceted nature of the objects. The intersection with the common $1/e$ threshold determining the resolution is shown in Table 1. The resolution normal to the flat faces is 2 nm or better for all samples, while the resolution is relatively low, far from any strong streaks in Fourier space. This angle-dependent resolution is a property of the diffractive-domain averaging before phase retrieval, but also due to the strongly faceted shape and lack of internal structure of these objects, both of which are not representative of biological objects.

5. CONCLUSION

We have demonstrated an order-of-magnitude increase in data collection efficiency along with much higher imaging resolution than previously achieved for x-ray single particle diffractive imaging, setting a template for future SPI experiments at the European XFEL and elsewhere. We have also shown that with these large data sets, one can structurally sort the particles and average a narrow size and shape range to obtain higher resolution. A similar problem is expected to be faced when imaging biological particles, and the method developed here shows the way towards overcoming conformational variability in the Fourier domain.

Although we benefited from the strong scattering cross section of gold compared to organic materials, with the commissioning of a sub-micrometer focus at the SPB/SFX instrument, we can expect comparable signal strengths from organic materials. Unfortunately, smaller x-ray foci would also mean lower hit ratios with the current sample delivery setup. Improvements could be made through optimized focusing for the targeted size distribution [17] or cryogenic injection systems [19] that additionally allow conformational selection [33]. Another approach is to keep using the larger focus and conjugate the particles with AuNPs to assist hitfinding and orientation determination [34]. The effective hit rate can also be increased by using more pulses in each train from the European XFEL (max. 2700) than the AGIPD detector can save (max. 352) and vetoing in real time those frames that do not contain diffraction signal.

The class of experiments exemplified here can also be applied to study rare events such as transient states in a spontaneous phase transition or high-free-energy states. Since each image is collected serially, one can identify relevant subsets corresponding to interesting states without averaging over all patterns. In this work, we have taken the approach of treating the objects as general 3D contrast functions with no *a priori* information. One can also envision a parameterized refinement approach that should enable a finer characterization of the structural landscape of the ensemble. Another direction for future development is the automatic classification of 2D intensity models to find the ones that correspond to single, non-spherical particles. In addition to improving the efficiency of the applications mentioned above, this would also enable the study of highly heterogeneous samples where the motifs themselves vary [35,36].

Funding. Deutsche Forschungsgemeinschaft (AIM, EXC 2056, ID 390715994, CUI, EXC 1074, ID 194651731); European Research Council (ERC-614507-Küpper); Helmholtz Association (Impuls-und Vernetzungsfond); Human Frontier Science Program (RGP0010/2017); Vetenskapsrådet; Carl

Tryggers Stiftelse för Vetenskaplig Forskning; Röntgen-Ångström Cluster; BioXFEL Science and Technology Center (STC-1231306); Joachim Herz Stiftung.

Acknowledgment. We thank Rick Millane for helpful discussions. We acknowledge European XFEL in Schenefeld, Germany, for provision of x-ray free-electron laser beamtime at Scientific Instrument SPB/SFX and thank the staff for their assistance. We thank the DESY NanoLab, CSSB cryoEM user facility and the XBI labs at EuXFEL for access to electron microscopy resources and their staff for their help. J.C.H.S. and R.A.K. acknowledge support from the National Science Foundation BioXFEL. J.R.N.C.M. acknowledges support from the Swedish Research Council, Röntgen-Ångström Cluster, and Carl Tryggers Foundation for Scientific Research. P.L.X. acknowledges a fellowship from the Joachim Herz Stiftung. P.L.X. and H.N.C. acknowledge support from the Human Frontiers Science Program.

Disclosures. The authors declare no conflicts of interest.

See Supplement 1 for supporting content.

[†]These authors contributed equally to this paper.

REFERENCES

1. R. Henderson, "The potential and limitations of neutrons, electrons and x-rays for atomic resolution microscopy of unstained biological molecules," Q. Rev. Biophys. **28**, 171–193 (1995).
2. R. Neutze, R. Wouts, D. Van der Spoel, E. Weckert, and J. Hajdu, "Potential for biomolecular imaging with femtosecond x-ray pulses," Nature **406**, 752–757 (2000).
3. H. N. Chapman, A. Barty, M. J. Bogan, S. Boutet, M. Frank, S. P. Hau-Riege, S. Marchesini, B. W. Woods, S. Bajt, W. H. Benner, R. A. London, E. Plönjes, M. Kuhlmann, R. Treusch, S. Düsterer, T. Tschentscher, J. R. Schneider, E. Spiller, T. Möller, C. Bostedt, M. Hoener, D. A. Shapiro, K. O. Hodgson, D. van der Spoel, F. Burmeister, M. Bergh, C. Caleman, G. Huldt, M. M. Seibert, F. R. N. C. Maia, R. W. Lee, A. Szöke, N. Timneanu, and J. Hajdu, "Femtosecond diffractive imaging with a soft-x-ray free-electron laser," Nat. Phys. **2**, 839–843 (2006).
4. A. Barty, C. Caleman, A. Aquila, N. Timneanu, L. Lomb, T. A. White, J. Andreasson, D. Arnlund, S. Bajt, T. R. M. Barends, M. Barthelmess, M. J. Bogan, C. Bostedt, J. D. Bozek, R. Coffee, N. Coppola, J. Davidsson, D. P. DePonte, R. B. Doak, T. Ekeberg, V. Elser, S. W. Epp, B. Erk, H. Fleckenstein, L. Foucar, P. Fromme, H. Graafsma, L. Gumprecht, J. Hajdu, C. Y. Hampton, R. Hartmann, A. Hartmann, G. Hauser, H. Hirsemann, P. Holl, M. S. Hunter, L. Johansson, S. Kassemeyer, N. Kimmel, R. A. Kirian, M. Liang, F. R. N. C. Maia, E. Malmerberg, S. Marchesini, A. V. Martin, K. Nass, R. Neutze, C. Reich, D. Rolles, B. Rudek, A. Rudenko, H. Scott, I. Schlichting, J. Schulz, M. M. Seibert, R. L. Shoeman, R. G. Sierra, H. Soltau, J. C. H. Spence, F. Stellato, S. Stern, L. Strüder, J. Ullrich, X. Wang, G. Weidenspointner, U. Weierstall, C. B. Wunderer, and H. N. Chapman, "Self-terminating diffraction gates femtosecond x-ray nanocrystallography measurements," Nat. Photonics **6**, 35–40 (2012).
5. C. Fortmann-Grote, A. Buzmakov, Z. Jurek, N.-T. D. Loh, L. Samoylova, R. Santra, E. A. Schneidmiller, T. Tschentscher, S. Yakubov, C. H. Yoon, M. V. Yurkov, B. Ziaja-Motyka, and A. P. Mancuso, "Start-to-end simulation of single-particle imaging using ultra-short pulses at the European x-ray free-electron laser," IUCrJ **4**, 560–568 (2017).
6. K. Ayyer, G. Geloni, V. Kocharyan, E. Saldin, S. Serkez, O. Yefanov, and I. Zagorodnov, "Perspectives for imaging single protein molecules with the present design of the European XFEL," Struct. Dyn. **2**, 041702 (2015).
7. K. Ayyer, A. J. Morgan, A. Aquila, H. DeMirci, B. G. Hogue, R. A. Kirian, P. L. Xavier, C. H. Yoon, H. N. Chapman, and A. Barty, "Low-signal limit of x-ray single particle diffractive imaging," Opt. Express **27**, 37816–37833 (2019).
8. M. J. Bogan, W. H. Benner, S. Boutet, U. Rohner, M. Frank, A. Barty, M. M. Seibert, F. Maia, S. Marchesini, S. Bajt, B. Woods, V. Riot, S. P. Hau-Riege, M. Svenda, E. Marklund, E. Spiller, J. Hajdu, and H. N. Chapman, "Single particle x-ray diffractive imaging," Nano Lett. **8**, 310–316 (2008).
9. M. M. Seibert, T. Ekeberg, F. R. N. C. Maia, M. Svenda, J. Andreasson, O. Jönsson, D. Odić, B. Iwan, A. Rocker, D. Westphal, M. Hantke, D. P. DePonte, A. Barty, J. Schulz, L. Gumprecht, N. Coppola, A. Aquila, M. Liang, T. A. White, A. Martin, C. Caleman, S. Stern, C. Abergel, V. Seltzer, J.-M. Claverie, C. Bostedt, J. D. Bozek, S. Boutet, A. A. Miahnahri, M. Messerschmidt, J. Krzywinski, G. Williams, K. O. Hodgson, M. J. Bogan, C. Y. Hampton, R. G. Sierra, D. Starodub, I. Andersson, S. Bajt, M. Barthelmess, J. C. H. Spence, P. Fromme, U. Weierstall, R. Kirian, M. Hunter, R. B. Doak, S. Marchesini, S. P. Hau-Riege, M. Frank, R. L. Shoeman, L. Lomb, S. W. Epp, R. Hartmann, D. Rolles, A. Rudenko, C. Schmidt, L. Foucar, N. Kimmel, P. Holl, B. Rudek, B. Erk, A. Hömke, C. Reich, D. Pietschner, G. Weidenspointner, L. Strüder, G. Hauser, H. Gorke, J. Ullrich, I. Schlichting, S. Herrmann, G. Schaller, F. Schopper, H. Soltau, K.-U. Kühnel, R. Andritschke, C.-D. Schröter, F. Krasniqi, M. Bott, S. Schorb, D. Rupp, M. Adolph, T. Gorkhover, H. Hirsemann, G. Potdevin, H. Graafsma, B. Nilsson, H. N. Chapman, and J. Hajdu, "Single mimivirus particles intercepted and imaged with an x-ray laser," Nature **470**, 78–81 (2011).
10. T. Ekeberg, M. Svenda, C. Abergel, F. R. N. C. Maia, V. Seltzer, J.-M. Claverie, M. Hantke, O. Jönsson, C. Nettelblad, G. van der Schot, M. Liang, D. P. DePonte, A. Barty, M. M. Seibert, B. Iwan, I. Andersson, N. D. Loh, A. V. Martin, H. Chapman, C. Bostedt, J. D. Bozek, K. R. Ferguson, J. Krzywinski, S. W. Epp, D. Rolles, A. Rudenko, R. Hartmann, N. Kimmel, and J. Hajdu, "Three-dimensional reconstruction of the giant mimivirus particle with an x-ray free-electron laser," Phys. Rev. Lett. **114**, 098102 (2015).
11. A. Munke, J. Andreasson, A. Aquila, S. Awel, K. Ayyer, A. Barty, R. J. Bean, P. Berntsen, J. Bielecki, S. Boutet, M. Bucher, H. N. Chapman, B. J. Daurer, H. DeMirci, V. Elser, P. Fromme, J. Hajdu, M. F. Hantke, A. Higashiura, B. G. Hogue, A. Hosseinizadeh, Y. Kim, R. A. Kirian, H. K. N. Reddy, T.-Y. Lan, D. S. D. Larsson, H. Liu, N. D. Loh, F. R. N. C. Maia, A. P. Mancuso, K. Mühlig, A. Nakagawa, D. Nam, G. Nelson, C. Nettelblad, K. Okamoto, A. Ourmazd, M. Rose, G. van der Schot, P. Schwander, M. M. Seibert, J. A. Sellberg, R. G. Sierra, C. Song, M. Svenda, N. Timneanu, I. A. Vartanyants, D. Westphal, M. O. Wiedorn, G. J. Williams, P. L. Xavier, C. H. Yoon, and J. Zook, "Coherent diffraction of single Rice Dwarf virus particles using hard x-rays at the Linac coherent light source," Sci. Data **3**, 160064 (2016).
12. H. K. Reddy, C. H. Yoon, A. Aquila, S. Awel, K. Ayyer, A. Barty, P. Berntsen, J. Bielecki, S. Bobkov, M. Bucher, G. A. Carini, S. Carron, H. Chapman, B. Daurer, H. DeMirci, T. Ekeberg, P. Fromme, J. Hajdu, M. F. Hanke, P. Hart, B. G. Hogue, A. Hosseinizadeh, Y. Kim, R. A. Kirian, R. P. Kurta, D. S. Larsson, N. Duane Loh, F. R. Maia, A. P. Mancuso, K. Mühlig, A. Munke, D. Nam, C. Nettelblad, A. Ourmazd, M. Rose, P. Schwander, M. Seibert, J. A. Sellberg, C. Song, J. C. Spence, M. Svenda, G. Van der Schot, I. A. Vartanyants, G. J. Williams, and P. L. Xavier, "Coherent soft x-ray diffraction imaging of coliphage PR772 at the Linac coherent light source," Sci. Data **4**, 170079 (2017).
13. I. V. Lundholm, J. A. Sellberg, T. Ekeberg, M. F. Hantke, K. Okamoto, G. van der Schot, J. Andreasson, A. Barty, J. Bielecki, P. Bruza, M. Bucher, S. Carron, B. J. Daurer, K. Ferguson, D. Hasse, J. Krzywinski, D. S. D. Larsson, A. Morgan, K. Mühlig, M. Müller, C. Nettelblad, A. Pietrini, H. K. N. Reddy, D. Rupp, M. Sauppe, M. Seibert, M. Svenda, M. Swiggers, N. Timneanu, A. Ulmer, D. Westphal, G. Williams, A. Zani, G. Faigel, H. N. Chapman, T. Möller, C. Bostedt, J. Hajdu, T. Gorkhover, and F. R. N. C. Maia, "Considerations for three-dimensional image reconstruction from experimental data in coherent diffractive imaging," IUCrJ **5**, 531–541 (2018).
14. E. Sobolev, S. Zolotarev, K. Giewekemeyer, J. Bielecki, K. Okamoto, H. K. N. Reddy, J. Andreasson, K. Ayyer, I. Barak, S. Bari, A. Barty, R. Bean, S. Bobkov, H. N. Chapman, G. Chojnowski, B. J. Daurer, K. Dörner, T. Ekeberg, L. Flückiger, O. Galzitskaya, L. Gelisio, S. Hauf, B. G. Hogue, D. A. Horke, A. Hosseinizadeh, V. Ilyin, C. Jung, C. Kim, Y. Kim, R. A. Kirian, H. Kirkwood, O. Kulyk, J. Küpper, R. Letrun, N. D. Loh, K. Lorenzen, M. Messerschmidt, K. Mühlig, A. Ourmazd, N. Raab, A. V. Rode, M. Rose, A. Round, T. Sato, R. Schubert, P. Schwander, J. A. Sellberg, M. Sikorski, A. Silenzi, C. Song, J. C. H. Spence, S. Stern, J.

Sztuk-Dambietz, A. Teslyuk, N. Timneanu, M. Trebbin, C. Uetrecht, B. Weinhausen, G. J. Williams, P. L. Xavier, C. Xu, I. A. Vartanyants, V. S. Lamzin, A. Mancuso, and F. R. N. C. Maia, "Megahertz single-particle imaging at the European XFEL," Commun. Phys. **3**, 97 (2020).
15. W. Decking, S. Abeghyan, P. Abramian, A. Abramsky, A. Aguirre, C. Albrecht, P. Alou, M. Altarelli, P. Altmann, K. Amyan, V. Anashin, E. Apostolov, K. Appel, D. Auguste, V. Ayvazyan, S. Baark, F. Babies, N. Baboi, P. Bak, V. Balandin, R. Baldinger, B. Baranasic, S. Barbanotti, O. Belikov, V. Belokurov, L. Belova, V. Belyakov, S. Berry, M. Bertucci, B. Beutner, A. Block, M. Blöcher, T. Böckmann, C. Bohm, M. Böhnert, V. Bondar, E. Bondarchuk, M. Bonezzi, P. Borowiec, C. Bösch, U. Bösenberg, A. Bosotti, R. Böspflug, M. Bousonville, E. Boyd, Y. Bozhko, A. Brand, J. Branlard, S. Briechle, F. Brinker, S. Brinker, R. Brinkmann, S. Brockhauser, O. Brovko, H. Brück, A. Brüdgam, L. Butkowski, T. Büttner, J. Calero, E. Castro-Carballo, G. Cattalanotto, J. Charrier, J. Chen, A. Cherepenko, V. Cheskidov, M. Chiodini, A. Chong, S. Choroba, M. Chorowski, D. Churanov, W. Cichalewski, M. Clausen, W. Clement, C. Cloué, J. A. Cobos, N. Coppola, S. Cunis, K. Czuba, M. Czwalinna, B. D'Almagne, J. Dammann, H. Danared, A. de Zubiaurre Wagner, A. Delfs, T. Delfs, F. Dietrich, T. Dietrich, M. Dohlus, M. Dommach, A. Donat, X. Dong, N. Doynikov, M. Dressel, M. Duda, P. Duda, H. Eckoldt, W. Ehsan, J. Eidam, and F. Eints, et al., "A MHz-repetition-rate hard x-ray free-electron laser driven by a superconducting linear accelerator," Nat. Photonics **14**, 391–397 (2020).
16. N.-T. D. Loh and V. Elser, "Reconstruction algorithm for single-particle diffraction imaging experiments," Phys. Rev. E **80**, 026705 (2009).
17. N. Roth, S. Awel, D. A. Horke, and J. Küpper, "Optimizing aerodynamic lenses for single-particle imaging," J. Aerosol Sci. **124**, 17–29 (2018).
18. J. Bielecki, M. F. Hantke, B. J. Daurer, H. K. N. Reddy, D. Hasse, D. S. D. Larsson, L. H. Gunn, M. Svenda, A. Munke, J. A. Sellberg, L. Flueckiger, A. Pietrini, C. Nettelblad, I. Lundholm, G. Carlsson, K. Okamoto, N. Timneanu, D. Westphal, O. Kulyk, A. Higashiura, G. van der Schot, N.-T. D. Loh, T. E. Wysong, C. Bostedt, T. Gorkhover, B. Iwan, M. M. Seibert, T. Osipov, P. Walter, P. Hart, M. Bucher, A. Ulmer, D. Ray, G. Carini, K. R. Ferguson, I. Andersson, J. Andreasson, J. Hajdu, and F. R. N. C. Maia, "Electrospray sample injection for single-particle imaging with x-ray lasers," Sci. Adv. **5**, eaav8801 (2019).
19. A. K. Samanta, M. Amin, A. D. Estillore, N. Roth, L. Worbs, D. A. Horke, and J. Küpper, "Controlled beams of shock-frozen, isolated, biological and artificial nanoparticles," Struct. Dyn. **7**, 024304 (2020).
20. A. P. Mancuso, A. Aquila, L. Batchelor, R. J. Bean, J. Bielecki, G. Borchers, K. Doerner, K. Giewekemeyer, R. Graceffa, O. D. Kelsey, Y. Kim, H. J. Kirkwood, A. Legrand, R. Letrun, B. Manning, L. Lopez Morillo, M. Messerschmidt, G. Mills, S. Raabe, N. Reimers, A. Round, T. Sato, J. Schulz, C. Signe Takem, M. Sikorski, S. Stern, P. Thute, P. Vagovič, B. Weinhausen, and T. Tschentscher, "The single particles, clusters and biomolecules and serial femtosecond crystallography instrument of the European XFEL: initial installation," J. Synchrotron Radiat. **26**, 660–676 (2019).
21. B. Henrich, J. Becker, R. Dinapoli, P. Goettlicher, H. Graafsma, H. Hirsemann, R. Klanner, H. Krueger, R. Mazzocco, A. Mozzanica, H. Perrey, G. Potdevin, B. Schmitt, X. Shi, A. Srivastava, U. Trunk, and C. Youngman, "The adaptive gain integrating pixel detector AGIPD a detector for the European XFEL," Nucl. Instrum. Methods Phys. A **633**, S11–S14 (2011).
22. S. Awel, R. A. Kirian, N. Eckerskorn, M. Wiedorn, D. A. Horke, A. V. Rode, J. Küpper, and H. N. Chapman, "Visualizing aerosol-particle injection for diffractive-imaging experiments," Opt. Express **24**, 6507–6521 (2016).
23. M. F. Hantke, J. Bielecki, O. Kulyk, D. Westphal, D. S. Larsson, M. Svenda, H. K. Reddy, R. A. Kirian, J. Andreasson, J. Hajdu, and F. R. N. C. Maia, "Rayleigh-scattering microscopy for tracking and sizing nanoparticles in focused aerosol beams," IUCrJ **5**, 673–680 (2018).
24. M. Rose, S. Bobkov, K. Ayyer, R. P. Kurta, D. Dzhigaev, Y. Y. Kim, A. J. Morgan, C. H. Yoon, D. Westphal, J. Bielecki, J. A. Sellberg, G. Williams, F. R. Maia, O. M. Yefanov, V. Ilyin, A. P. Mancuso, H. N. Chapman, B. G. Hogue, A. Aquila, A. Barty, and I. A. Vartanyants, "Single-particle imaging without symmetry constraints at an x-ray free-electron laser," IUCrJ **5**, 727–736 (2018).
25. S. H. Scheres, M. Valle, R. Nuñez, C. O. Sorzano, R. Marabini, G. T. Herman, and J.-M. Carazo, "Maximum-likelihood multi-reference refinement for electron microscopy images," J. Mol. Biol. **348**, 139–149 (2005).
26. N. D. Loh, M. J. Bogan, V. Elser, A. Barty, S. Boutet, S. Bajt, J. Hajdu, T. Ekeberg, F. R. N. C. Maia, J. Schulz, M. M. Seibert, B. Iwan, N. Timneanu, S. Marchesini, I. Schlichting, R. L. Shoeman, L. Lomb, M. Frank, M. Liang, and H. N. Chapman, "Cryptotomography: reconstructing 3D Fourier intensities from randomly oriented single-shot diffraction patterns," Phys. Rev. Lett. **104**, 225501 (2010).
27. K. Ayyer, T.-Y. Lan, V. Elser, and N. D. Loh, "Dragonfly: an implementation of the expand–maximize–compress algorithm for single-particle imaging," J. Appl. Crystallogr. **49**, 1320–1335 (2016).
28. H. T. Philipp, K. Ayyer, M. W. Tate, V. Elser, and S. M. Gruner, "Solving structure with sparse, randomly-oriented x-ray data," Opt. Express **20**, 13129–13137 (2012).
29. K. Giewekemeyer, A. Aquila, N.-T. D. Loh, Y. Chushkin, K. S. Shanks, J. Weiss, M. W. Tate, H. T. Philipp, S. Stern, P. Vagovic, M. Mehrjoo, C. Teo, M. Barthelmess, F. Zontone, C. Chang, R. C. Tiberio, A. Sakdinawat, G. J. Williams, S. M. Gruner, and A. P. Mancuso, "Experimental 3D coherent diffractive imaging from photon-sparse random projections," IUCrJ **6**, 357–365 (2019).
30. P. J. Ho, B. J. Daurer, M. F. Hantke, J. Bielecki, A. Al Haddad, M. Bucher, G. Doumy, K. R. Ferguson, L. Flückiger, T. Gorkhover, B. Iwan, C. Knight, S. Moeller, T. Osipov, D. Ray, S. H. Southworth, M. Svenda, N. Timneanu, A. Ulmer, P. Walter, J. Hajdu, L. Young, F. R. N. C. Maia, and C. Bostedt, "The role of transient resonances for ultra-fast imaging of single sucrose nanoclusters," Nat. Commun. **11**, 167 (2020).
31. N. D. Loh, D. Starodub, L. Lomb, C. Y. Hampton, A. V. Martin, R. G. Sierra, A. Barty, A. Aquila, J. Schulz, J. Steinbrener, R. L. Shoeman, S. Kassemeyer, C. Bostedt, J. Bozek, S. W. Epp, B. Erk, R. Hartmann, D. Rolles, A. Rudenko, B. Rudek, L. Foucar, N. Kimmel, G. Weidenspointner, G. Hauser, P. Holl, E. Pedersoli, M. Liang, M. S. Hunter, L. Gumprecht, N. Coppola, C. Wunderer, H. Graafsma, F. R. Maia, T. Ekeberg, M. Hantke, H. Fleckenstein, H. Hirsemann, K. Nass, T. A. White, H. J. Tobias, G. R. Farquar, W. H. Benner, S. Hau-Riege, C. Reich, A. Hartmann, H. Soltau, S. Marchesini, S. Bajt, M. Barthelmess, L. Strueder, J. Ullrich, P. Bucksbaum, M. Frank, I. Schlichting, H. N. Chapman, and M. J. Bogan, "Sensing the wavefront of x-ray free-electron lasers using aerosol spheres," Opt. Express **21**, 12385–12394 (2013).
32. T.-Y. Lan, J. L. Wierman, M. W. Tate, H. T. Philipp, V. Elser, and S. M. Gruner, "Reconstructing three-dimensional protein crystal intensities from sparse unoriented two-axis x-ray diffraction patterns," J. Appl. Crystallogr. **50**, 985–993 (2017).
33. Y.-P. Chang, D. A. Horke, S. Trippel, and J. Küpper, "Spatially-controlled complex molecules and their applications," Int. Rev. Phys. Chem. **34**, 557–590 (2015).
34. K. Ayyer, "Reference-enhanced x-ray single-particle imaging," Optica **7**, 593–601 (2020).
35. I. Barke, H. Hartmann, D. Rupp, L. Flückiger, M. Sauppe, M. Adolph, S. Schorb, C. Bostedt, R. Treusch, C. Peltz, S. Bartling, T. Fennel, K.-H. Meiwes-Broer, and T. Möller, "The 3D-architecture of individual free silver nanoparticles captured by x-ray scattering," Nat. Commun. **6**, 6187 (2015).
36. B. Langbehn, K. Sander, Y. Ovcharenko, C. Peltz, A. Clark, M. Coreno, R. Cucini, M. Drabbels, P. Finetti, M. Di Fraia, L. Giannessi, C. Grazioli, D. Iablonskyi, A. C. LaForge, T. Nishiyama, V. Oliver Álvarez de Lara, P. Piseri, O. Plekan, K. Ueda, J. Zimmermann, K. C. Prince, F. Stienkemeier, C. Callegari, T. Fennel, D. Rupp, and T. Möller, "Three-dimensional shapes of spinning helium nanodroplets," Phys. Rev. Lett. **121**, 255301 (2018).